Geophysical Research Letters]

Supporting Information for

Radial and azimuthal anisotropy tomography of the NE Japan subduction zone: implications for the Pacific slab subduction dynamics

Motoko Ishise[1], Hitoshi Kawakatsu[1], Manabu Morishige[2], Katsuhiko Shiomi[3]

1 The University of Tokyo, Tokyo, Japan

2 Japan Agency for Marin-Earth Science and Technology, Yokohama, Japan

3 National Research Institute for Earth Science and Disaster Resilience, Tsukuba, Japan

Contents of this file

Introduction

Text S1 describes P wave velocity in anisotropic medium. The description is used in the anisotropic tomography inversion. Text S2 shows how to evaluate apparent anisotropy caused by dip of the anisotropy symmetry axis. Figures S1-S5 are dataset used in the anisotropy tomography analyses, resultant P wave anisotropy structures, and results of checker board resolution tests. Table S1 indicate locations of grid points.

Text S1.

P-wave velocity in anisotropic medium

P-wave velocity propagating in weakly anisotropic media is expressed as

$$V = v_0(1 + A + B\cos 2\alpha + E\cos 4\alpha) \quad \text{(A1)}$$

where α is the angle between the symmetry axis and ray vector, A is the dimensionless perturbation of a reference isotropic velocity v_0. B and E are the dimensionless parameters to describe the seismic anisotropy (Backus, 1965). In the lithospheric mantle and crust, the $\cos 4\,\alpha$ term is negligibly small in comparison with other terms (e.g., Raitt et al., 1969; Kaneshima, 1990). Therefore, (A1) can be approximated by equation (A2).

$$V = v_0(1 + A + B\cos 2\alpha) \quad \text{(A2)}$$

Note that this incidence angle dependence of P wave velocity is equivalent to that of weak anisotropy of transversely isotropic media with elliptic condition (Kawakatsu et al., 2015; Thomsen, 1986).

In the case of azimuthal anisotropy medium, where hexagonal symmetry axis is assumed to be in the horizontal plane, the angle between symmetry axis and ray vector, α, is written as $\cos\alpha = \sin i \sin\phi \sin\theta + \sin i \cos\phi \cos\theta$, following the coordinate system of Ishise & Oda (2005). θ denotes the azimuth of the hexagonal symmetry axis, ϕ and i are the azimuth and incident angle of the ray. Therefore, P wave velocity propagating in the azimuthal anisotropy medium is written by following the equation,

$$V = v_0 + v_0 A + v_0 B(\sin i)^2 \{1 + \cos 2(\phi - \theta)\}. \quad \text{(A3)}$$

In the azimuthal anisotropy tomographic inversion, v_0, i, ϕ are known parameter, and then A, B, θ are the unknown parameters.

In the case of radial anisotropy analysis, the hexagonal symmetry axis is assumed to be vertical, so the angle between the hexagonal symmetry axis and ray vector, α, is equal to the incident angle of the ray vector, i. Therefore, P wave velocity propagating in radial anisotropic media is expressed by

$$V = v_0(1 + A + B\cos 2i). \quad \text{(A4)}$$

Where, v_0, i, ϕ are known parameter, and A and B are the unknown parameters. Then, in the radial anisotropy tomographic inversion, we calculate A and B in order to minimize travel-time residuals with damped least squares method.

Text S2.

Apparent azimuthal and radial anisotropy due to tilted transverse isotropy (TTI)

We need to evaluate how a medium with hexagonal symmetry with tilted symmetry axis is "observed" as an average in azimuthal and radial travel time tomography. As above, we assume weak anisotropy of transversely isotropy with the elliptic condition. Then the incidence angle dependence of P wave velocity can be given in a similar form to (A1) as,

$$V = a + b\cos 2\alpha. \qquad \text{(A5)}$$

Let us assume that the symmetry axis is tilted to an arbitrary direction denoted by a unit vector **s** = (s_x, s_y, s_z) with z-axis being vertical. Then the azimuthal average of P wave propagation velocity in the horizontal plane is $V_H = a-b*s_z^2$, and the velocity in the vertical direction is $V_V = (a-b) +2b*s_z^2$. So, if this system is observed via radial tomography, the strength of apparent anisotropy becomes,

$$RA^a = 2\frac{(V_H - V_V)}{(V_H + V_V)} = \frac{b(3s_z^2-1)}{a-\frac{b}{2}(1-s_z^2)} \qquad \text{(A6)}$$

The strength of azimuthal anisotropy in the horizontal plane can be expressed as

$$AA^a = \frac{b}{a}\frac{(1-s_z)}{(1-\frac{b}{a}s_z)} \qquad \text{(A7)}$$

where the strength gives half of peak-to-peak anisotropy, and the direction of the symmetry axis is given by $\tan^{-1}(s_y/s_x)$.

Using (A6) and (A7), we can evaluate the effect of dip on an arbitrary TTI medium. For a case that the TTI system is dipped by an angle δ, assuming the dip (rotation) of the system occurs around the y-axis, the symmetry axis in the dipped system is given by a unit vector

$$s' = \begin{pmatrix} s_x cos\,\delta - s_z sin\,\delta \\ s_y \\ s_x sin\,\delta + s_z cos\,\delta \end{pmatrix} \qquad \text{(A8)}$$

So, we can use $\boldsymbol{s'}$, instead of $\boldsymbol{s}$, in the expressions given above (A6) and (A7). For the particular example shown in Figure 5, the original (zero dip) anisotropy is given by either VTI (radial anisotropy due to laminar structure) or HTI (azimuthal anisotropy due to LPO at spreading; the fast direction rotated -30° relative to the slab strike: *cf.* Figure 1).

References

Backus, G.E. (1965), Possible forms of seismic anisotropy of the upper-most mantle under oceans, J. Geophys. Res., 70, 3429-3439.

Ishise, M., & H. Oda (2005), Three-dimensional structure of P-wave anisotropy beneath Tohoku district, northeast Japan, J. Geophys. Res., 110, doi: 10.1029/2004JB003599.

Kaneshima, S. (1990), Origin of crustal anisotropy: shear wave splitting studies in Japan, J. Geophys. Res., 95, 11121-11133.

Kawakatsu, H., J.-P. Montagner, & T.-R. A. Song (2015), On DLA's &eta, *GSA Special Paper 514: The Interdisciplinary Earth: A Volume in Honor of Don L. Anderson (edited by G. Foulger et al.)*, pp. 33-38.

Raitt, R.W., G.G. Shore Jr., T.J.G. Fransis, & G.B. Morris (1969), Anisotropy of the Pacific upper mantle, J. Geophys. Res., 74, 3095-3109.

Thomsen, L., 1986. Weak elastic anisotropy. Geophysics 51, 1954–1966.

Figure S1(a).

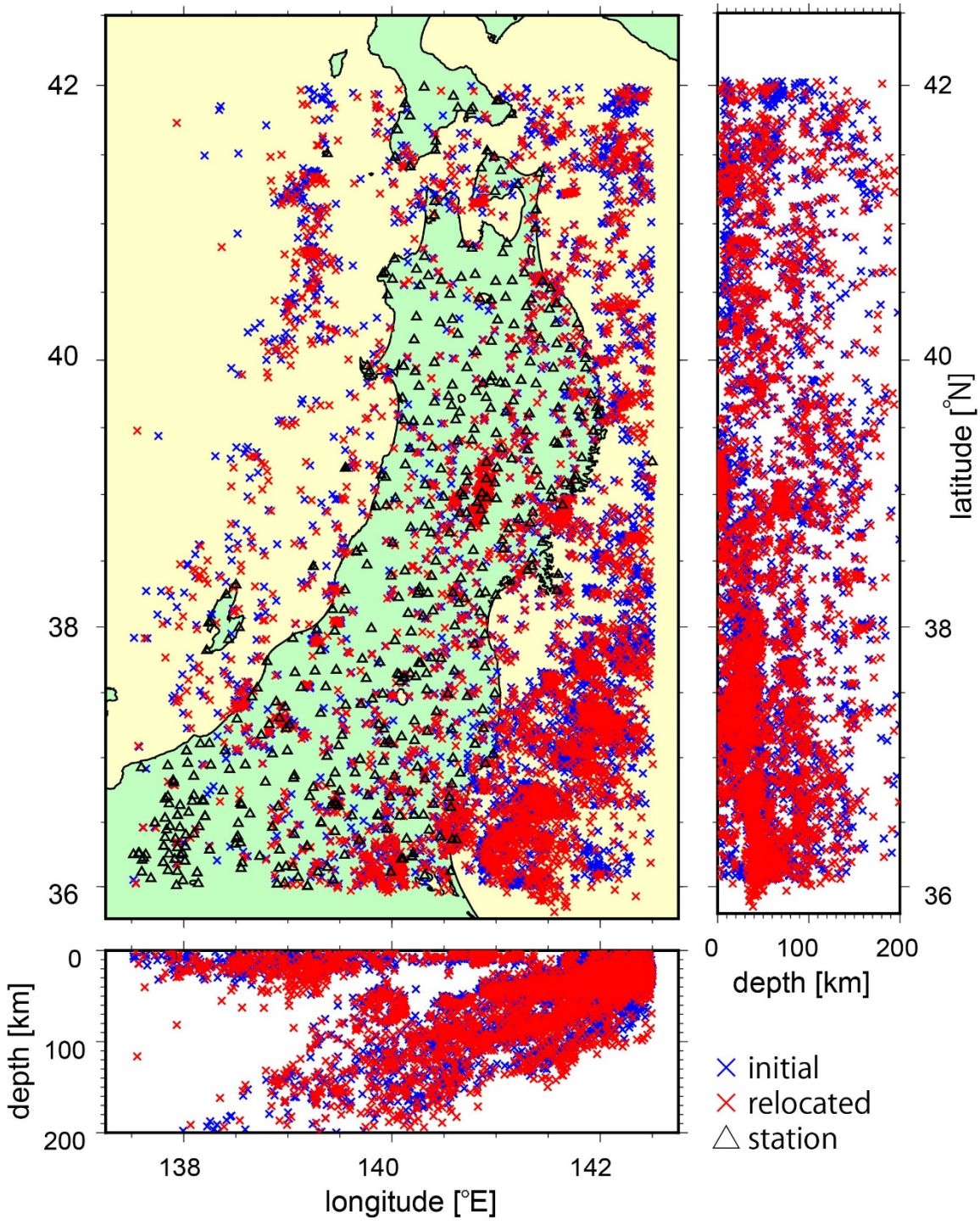
42
40
38
36
0
100
200
depth [km]
latitude [°N]
138
140
142
longitude [°E]
initial
relocated
station

Figure S1(b).

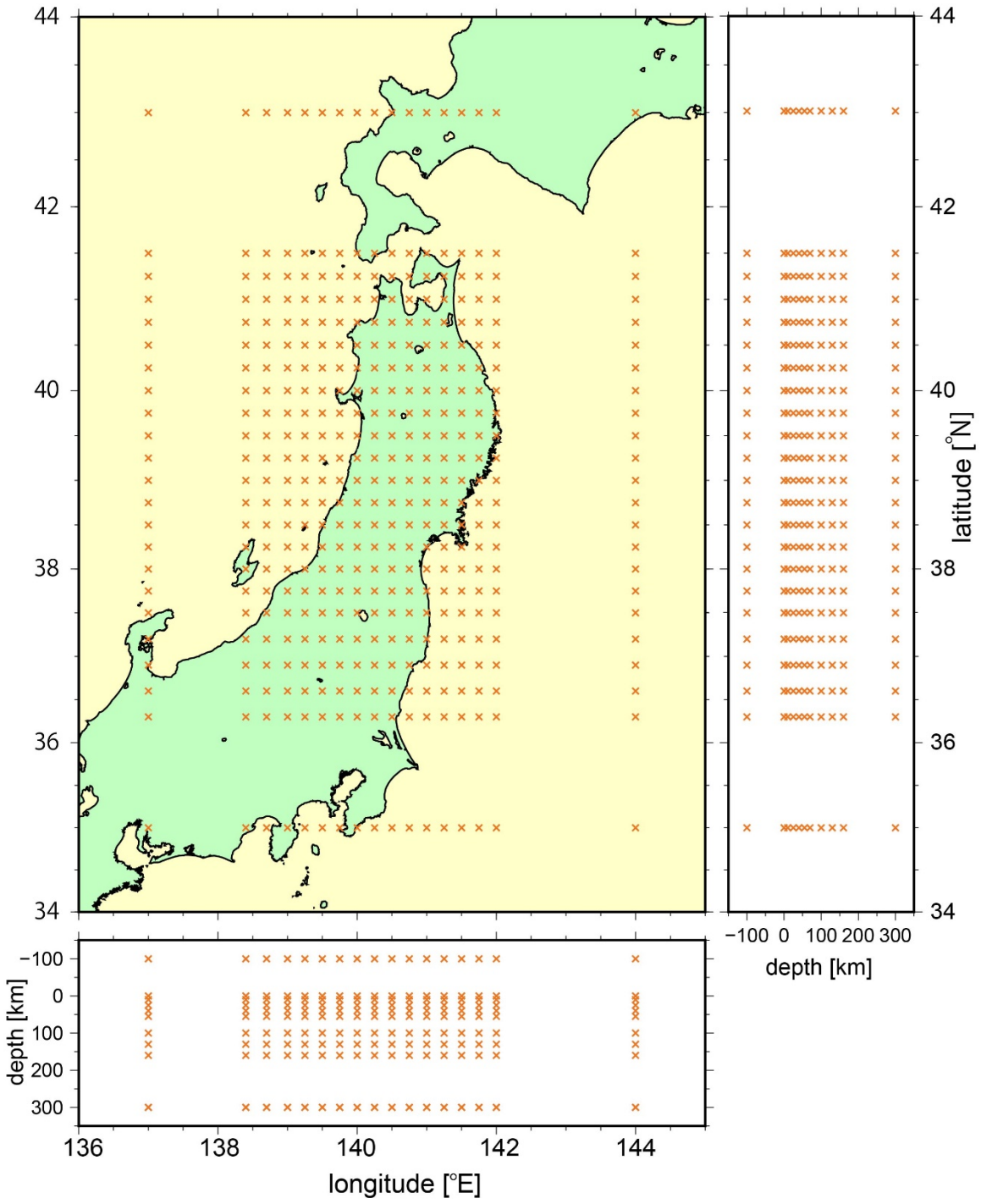
44
42
40
38
36
34
136
138
140
142
144
longitude [°E]
latitude [°N]
depth [km]
−100
0
100
200
300
−100 0 100 200 300
depth [km]

Figure S1(c).

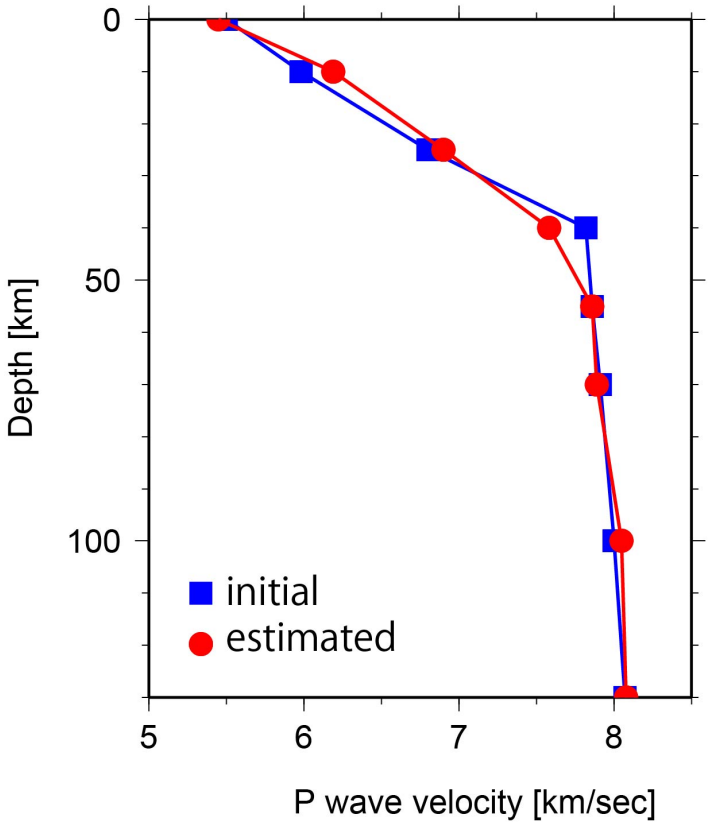

Figure S1. (a) Hypocenter distribution before and after 1D inversion. Blue and red crosses represent initial and relocated hypocenters, respectively. Black triangles show seismic stations used in this study. (b) Orange crosses indicate a grid configuration used to represent 3D anisotropic velocity structure. (c) Initial and estimated 1D velocity structures by simultaneous inversion of 1D velocity structure and hypocenter relocation. The starting model is made based on a standard isotropic velocity model (Ukawa et al., 1984).

Figure S2.

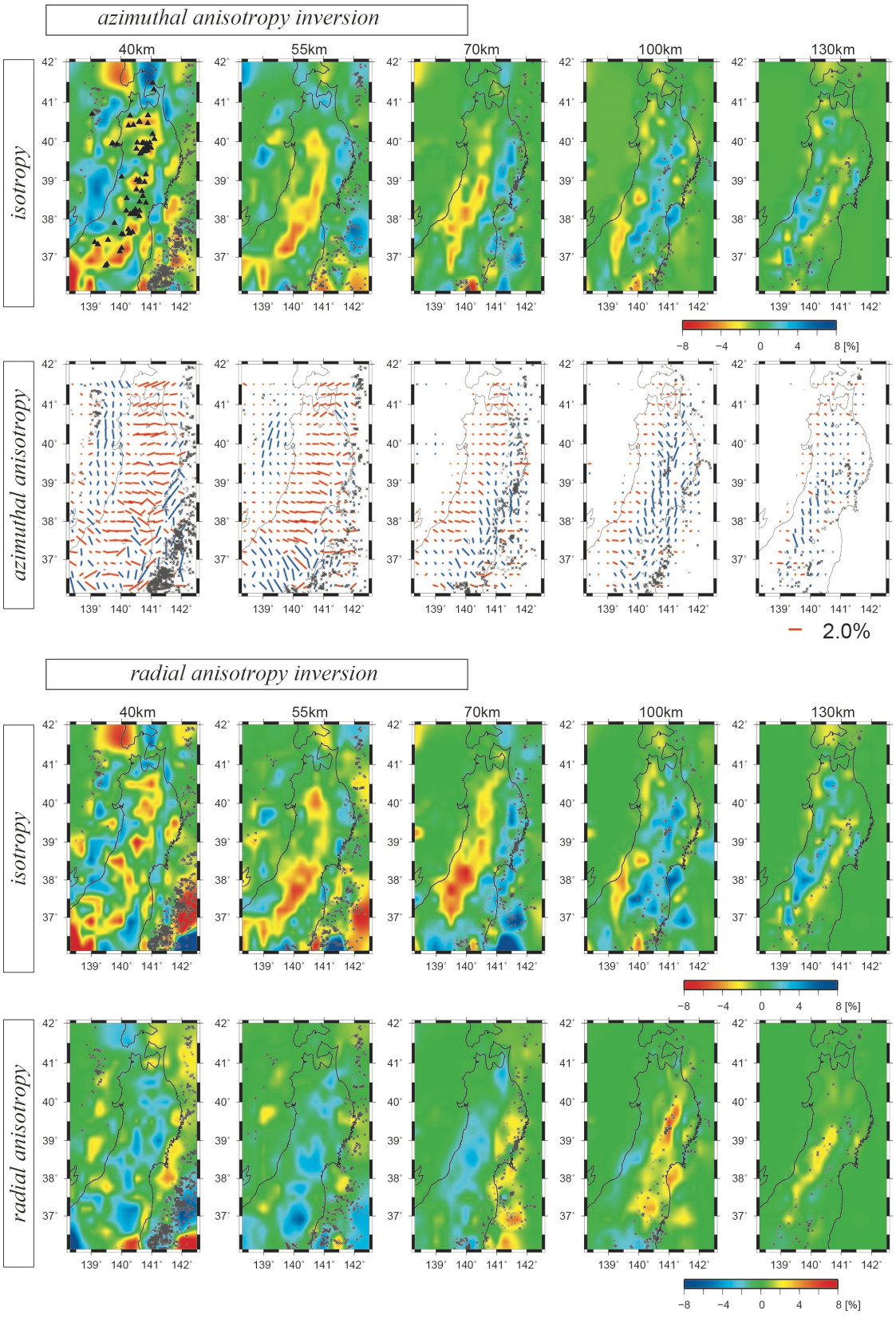
azimuthal anisotropy inversion
40km
55km
70km
100km
130km
isotropy
azimuthal anisotropy
−8 −4 0 4 8 [%]
2.0%
radial anisotropy inversion
radial anisotropy

Figure S2. Lateral variations of azimuthal and radial anisotropic velocity at depths deeper than 40 km depth. (upper) Isotropic velocity and azimuthal anisotropy obtained by azimuthal anisotropy (AA) inversion. Strength and fast propagation direction of azimuthal anisotropy are represented by length and direction of the bar. The color of bars indicates a trend of fast propagation direction: blue means that the fast direction is N–S trending, and red means that the fast direction is E–W trending. (lower) Isotropic velocity and radial anisotropy obtained by radial anisotropy (RA) inversion. Isotropic and radial anisotropy velocity perturbations are shown by a color scale at the bottom left. Black triangles represent active volcanoes. Crosses are earthquakes relocated within less than 5 km from each depth.

Figure S3.

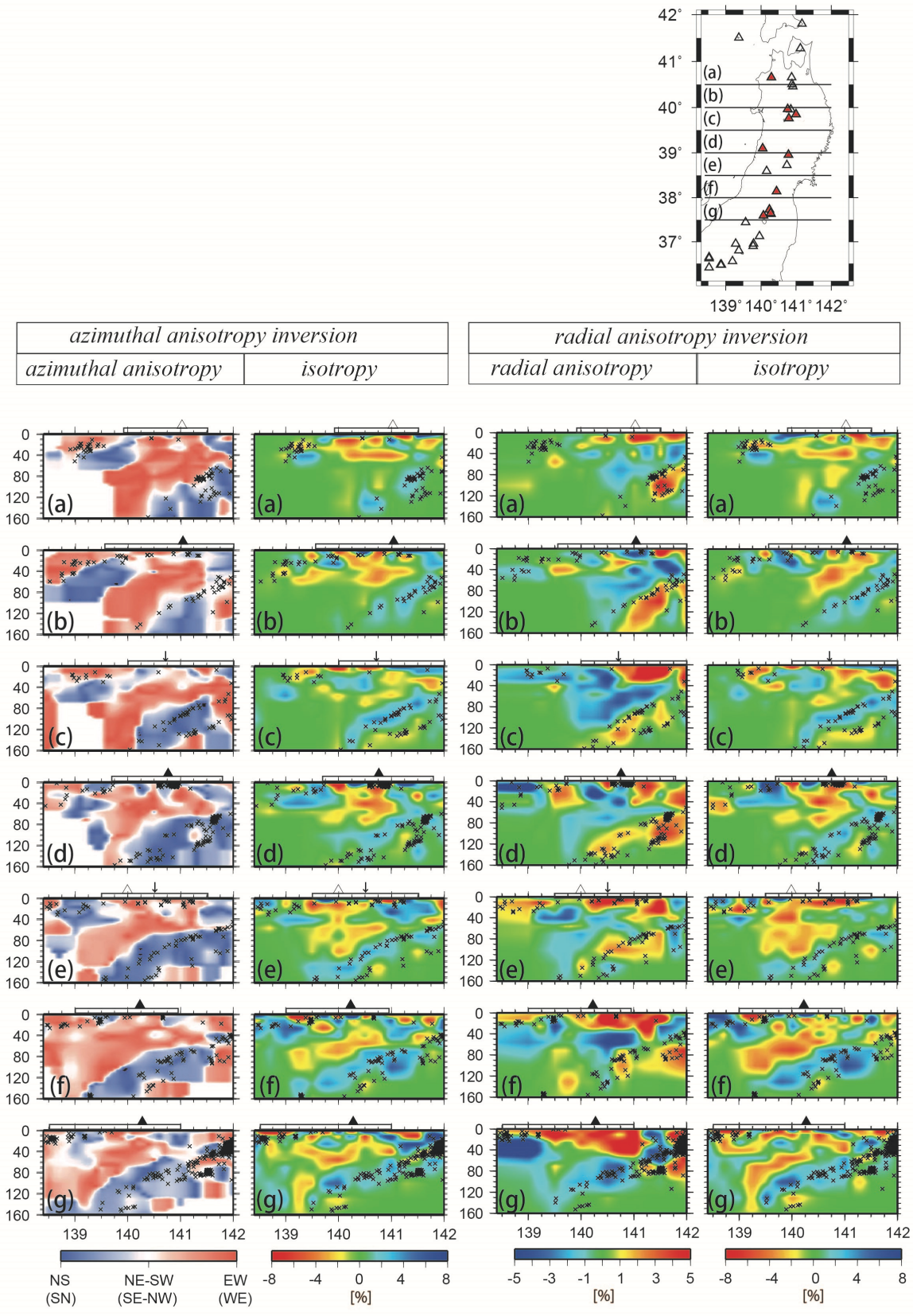
42°
41°
40°
39°
38°
37°
(a)
(b)
(c)
(d)
(e)
(f)
(g)
139° 140° 141° 142°
azimuthal anisotropy inversion
azimuthal anisotropy
isotropy
radial anisotropy inversion
radial anisotropy
isotropy
0
40
80
120
160
139
140
141
142
NS
(SN)
NE-SW
(SE-NW)
EW
(WE)
-8
-4
0
4
8
[%]
-5
-3
-1
1
3
5

Figure S3. Vertical cross sections of azimuthal and radial anisotropic velocity structure. (left panel) vertical cross sections of isotropic velocity and azimuthal anisotropy obtained from azimuthal anisotropy tomography inversion. (right panel) vertical cross sections of isotropic velocity and radial anisotropic velocity structure obtained from radial anisotropy tomography inversion. White plates indicate land area. Locations of active and inactive volcano are shown by solid and open triangles. Small arrows indicate the location of volcanic front. Crosses are hypocenters within 10 km from the cross-sections.

The subducting Pacific slab is shown as a high-velocity anomaly in the isotropic tomography images. Also, it is characterized by N-S-trending azimuthal anisotropy and $V_{PH} > V_{PV}$ radial anisotropy in anisotropic tomography images. The Pacific slab in isotropic tomography images is more apparent than that in anisotropic tomography images. It indicates that isotopic velocity is robust and anisotropy is secondary.

In order to understand the mantle dynamics of the study area, melt behavior is important because it would control the magmatism of the subduction zone. There are two likely existence forms of melt in the mantle wedge of the subduction zone. One is a melt-filled dyke (dike filled with partially melted liquid) (e.g., Nur & Simmons, 1969; Zummerman et al., 1999), and the other is a melt-segregated shear zone (sheet-like structure) (Holzman et al., 2003). When there are preferentially oriented melt-filled dykes in the mantle wedge, they would create N–S-trending azimuthal anisotropy as is discussed in our previous study (Ishise and Oda, 2005). Also it will indicate $VP_V > VP_H$ radial anisotropy because the crack planes are vertical. On the other hand, if melt constructs a sheet-like structure in the mantle wedge, it would not show distinct azimuthal anisotropy but provide radial anisotropy with $VP_V < VP_H$. However, both expected characteristics of anisotropy can't explain the resultant anisotropy structure. Thus, the melt-related structure might constrain in a small area that cannot be detected by the tomography study.

Figure S4.

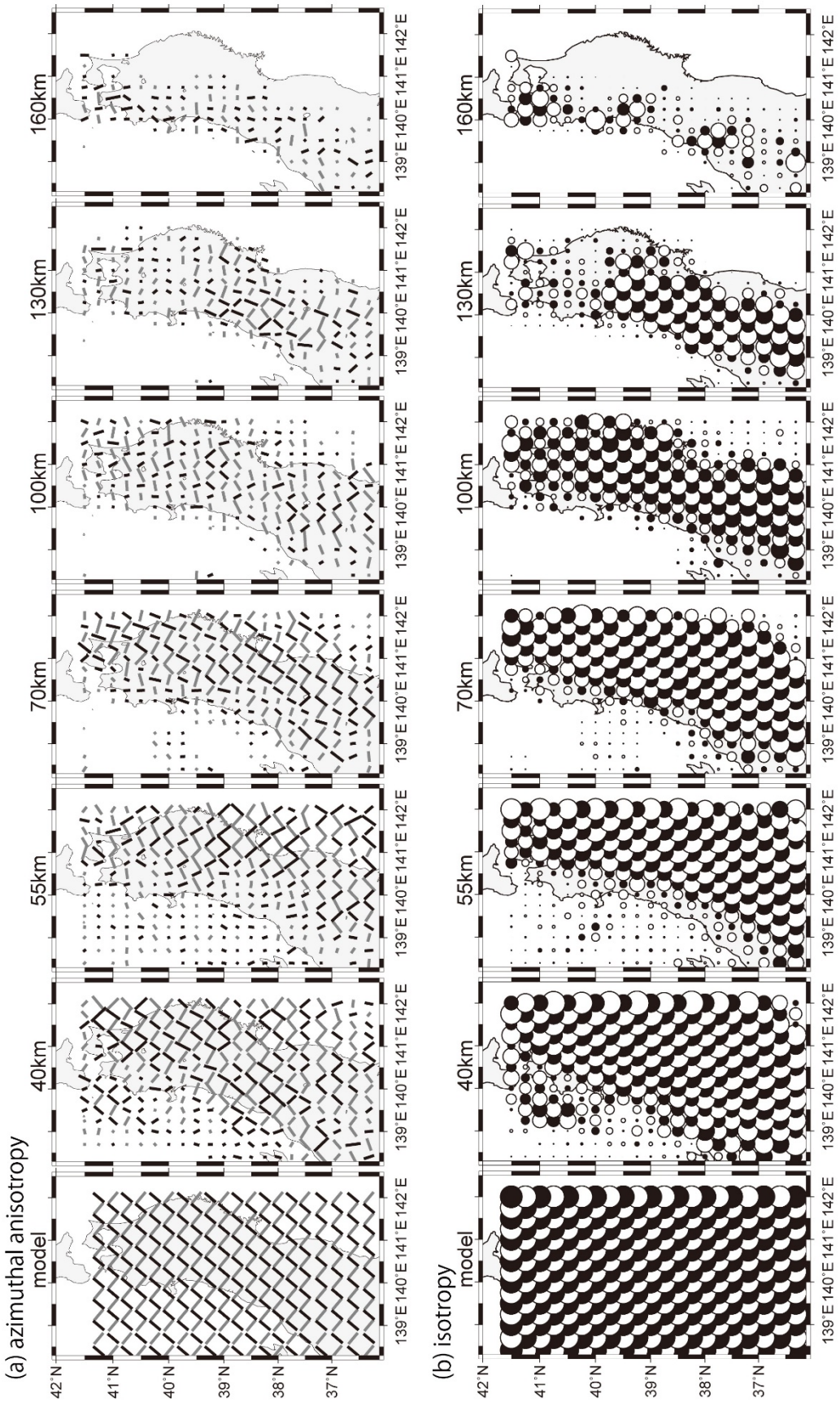
(a) azimuthal anisotropy
model
40km
55km
70km
100km
130km
160km
(b) isotropy
model
40km
55km
70km
100km
130km
160km
42°N
41°N
40°N
39°N
38°N
37°N
139°E
140°E
141°E
142°E

Figure S4. Results of the checker board resolution test of azimuthal anisotropy tomography in the mantle and slab region; (a) azimuthal anisotropy, (b) isotropic velocity. Isotropic and anisotropic velocity perturbations of P-waves used to produce the synthetic P-wave travel-time data are shown in the leftmost maps of (a) and (b), respectively. Lateral variations of 2 % isotropic velocity perturbation and 2 % and 40 degrees azimuthal anisotropy are given at 0, 25, 55, 100, and 160 km depths. The reverse pattern of (a) and 2 % and 130 degrees azimuthal anisotropy are given at 10, 40, 70, 130 km depths.

Figure S5.

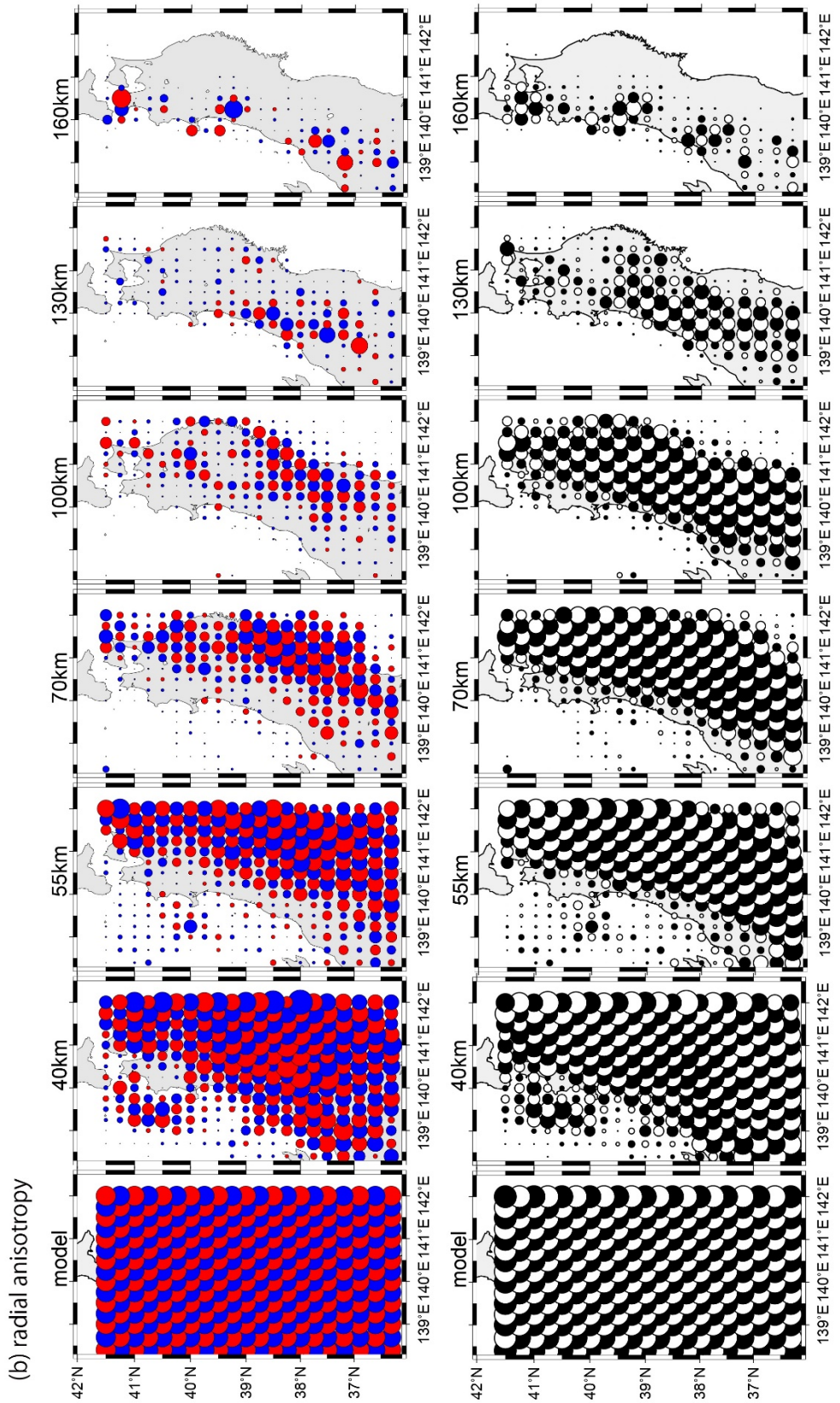
(b) radial anisotropy
model
40km
55km
70km
100km
130km
160km
42°N
41°N
40°N
39°N
38°N
37°N
139°E
140°E
141°E
142°E

Figure S5. Result of the checker board resolution test of radial anisotropy tomography in the mantle and slab region; (a) radial anisotropy, (b) isotropic velocity. Isotropic and anisotropic velocity perturbations of P-waves used to produce the synthetic P-wave travel-time data are shown in the leftmost map of (a) and (b), respectively. Lateral variations of 5 % isotropic velocity perturbation and 3 % radial anisotropy are given at 0, 25, 55, 100, and 160 km depths. The reverse patterns of (a) and (b) are given at 10, 40, 70, 130 km depths.

Table S1. Position of the grid points.

Position coordinate correspondence tables of 3D grid configuration

Latitude		Longitude		Depth	
grid #	latitude	grid #	longitude	grid #	depth
1	35.00	1	137.00	1	−100
2	36.30	2	138.40	2	0
3	36.60	3	138.70	3	10
4	36.90	4	139.00	4	25
5	37.20	5	139.25	5	40
6	37.50	6	139.50	6	55
7	37.75	7	139.75	7	70
8	38.00	8	140.00	8	100
9	38.25	9	140.25	9	130
10	38.50	10	140.50	10	160
11	38.75	11	140.75	11	300
12	39.00	12	141.00		
13	39.25	13	141.25		
14	39.50	14	141.50		
15	39.75	15	141.75		
16	40.00	16	142.00		
17	40.25	17	144.00		
18	40.50				
19	40.75				
20	41.00				
21	41.25				
22	41.50				
23	43.00				